Journal of the European Ceramic Society 44 (2024) 5646–5658

Contents lists available at ScienceDirect

Journal of the European Ceramic Society

journal homepage: www.elsevier.com/locate/jeurceramsoc

The role of Ca/Zr ratio on the local structure and phase transitions in lead-free (Ba,Ca)(Zr,Ti)O_3

David K. Dobesh [a,1], Ahmed Gadelmawla [a,b,*,1], Hidetoshi Miyazaki [b], Manuel Hinterstein [c,d], Koji Kimura [b,e], Juliana G. Maier [a], Semanti Banerjee [a], Omar Zeair [a], Sharly C. Mehta [a], Lucas Lemos da Silva [c,d], Neamul H. Khansur [a], Koichi Hayashi [a,e], Dominique de Ligny [a], Kyle G. Webber [a], Maria Rita Cicconi [a,*]

[a] Department of Materials Science and Engineering, Friedrich-Alexander-Universität Erlangen-Nürnberg (FAU), Erlangen 91058, Germany
[b] Department of Physical Science and Engineering, Nagoya Institute of Technology, Gokiso, Showa, Nagoya 466-8555, Japan
[c] Karlsruher Institut für Technologie, Institut für Angewandte Materialien, Karlsruhe 76131, Germany
[d] Fraunhofer IWM, Freiburg 79108, Germany
[e] Japan Synchrotron Radiation Research Institute, SPring-8, Sayo, Kouto 679-5198, Japan

ARTICLE INFO

Keywords:
BCZT
Raman spectroscopy
PDF
Functional ceramics
Phase transformations

ABSTRACT

In this study, the structural phase transitions are investigated as a function of composition and temperature for polycrystalline $x(Ba_{0.7}Ca_{0.3})TiO_3$-$(1-x)Ba(Zr_{0.2}Ti_{0.8})O_3$ (x = 0.40, 0.45, 0.50, 0.55, and 0.60) through a combination of Raman spectroscopy, synchrotron X-ray diffraction, and dielectric spectroscopy. The aim is to gain insight into the complex phase boundary region responsible for the excellent electromechanical properties. The results demonstrate the correlation between local site substitutions based on the stoichiometric variations to the microstructure and dielectric properties. The dielectric response has been correlated with the BCT/BZT content displaying a maximum depending on the phase content. Additionally, *in situ* temperature-dependent Raman, permittivity, and pair distribution function (PDF) studies were performed from −60 °C to 130 °C to highlight the structure and phase evolution. In particular, the *in situ* temperature-dependent Raman measurements reveal sudden discontinuities in the vibrational modes that correspond to the structural changes in the perovskite structure. Therefore, the results of the permittivity response, based on the average of a large volume, are consistent with the local structural changes obtained by other techniques. Indeed, correlations of Raman, X-ray diffraction, and PDFs obtained from synchrotron X-ray total scattering data, along with permittivity measurements allowed the identification of the discrete ferro- to paraelectric phase transitions and a more robust characterization. The rotation and distortion of the octahedral caused by oxygen displacement are driving forces behind symmetry changes and phase transitions, explaining the mechanism of polymorphic phase transition based on A- and B-site substitution. Therefore, this work provides a comprehensive understanding of temperature and composition-dependent phase transitions in BCZT.

1. Introduction

Functional ferroelectrics perovskites are an enabling material class used in numerous applications, such as actuators, sensors, energy storage, and electronic components. In particular, the generation of energy through the piezoelectric behavior of ceramics, *e.g.*, Pb(Zr,Ti)O_3, PZT, is of particular interest for energy harvesting systems [1–4]. Concerns about the environment increase the demand for clean energy by prohibiting the use of hazardous components [5]. Therefore, the development of lead-free ferroelectrics that can potentially replace PZT has been of special interest both academically and industrially [6–8]. Among all lead-free ferroelectrics, the BCZTx family $x(Ba_{0.7}Ca_{0.3})TiO_3$-$(1-x)Ba(Zr_{0.2}Ti_{0.8})O_3$ showed a remarkably high piezoelectric coefficient $d_{33} \approx$ 620 pC/N [9] and relatively low Curie temperature T_C within a range of

* Correspondence to: FAU - Friedrich-Alexander-Universität Erlangen-Nürnberg, Department Werkstoffwissenschaften, Lehrstuhl für Glas und Keramik (WW3), Martensstraße 5, Erlangen D-91058, Germany.
E-mail addresses: ahmed.gadelmawla@fau.de (A. Gadelmawla), maria.rita.cicconi@fau.de (M.R. Cicconi).
[1] Equal contribution

https://doi.org/10.1016/j.jeurceramsoc.2024.03.003
Received 2 November 2023; Received in revised form 19 February 2024; Accepted 1 March 2024
Available online 5 March 2024

~70–120 °C, depending on A-site ratio Ca/Ba in BCT and B-site ratio Zr/Ti in BZT as BCT/BZT ratio [10].

An improved understanding of the crystal structure, phase transitions, and compositional boundaries is critical for the observed electromechanical response and specific applications [11,12]. In particular, a large electric field-induced strain in the vicinity of the polymorphic phase boundaries (PPB) was reported for BCZT, although the origins of this response remain under debate [13]. Furthermore, the highest mechanical quality factor and small signal d_{33} was determined close to orthorhombic (O)-tetragonal (T) phase boundaries, where reduced anisotropy energy and increased softening occur, similar to the PZT system [11,14]. In addition to electromechanical properties, the coexistence of the intermediate O phase has also been related to high elastic compliance in BCZT45–55 at room temperature [15]. These data illustrate the sensitivity of the mechanical and electrical properties to change in the structure and phase boundaries.

Similar to the morphotropic phase boundaries MPB in PZT [16,17], the PPBs in BCZT were suggested to be responsible for the exceptional piezoelectric coupling [9]. Previous X-ray diffraction studies have reported the average crystal structure of BCZT as a function of temperature and composition [14,18–20]. The first reported phase diagram of BCZT showed only one interferroelectric phase transition between rhombohedral (R, *R*3*m*) and tetragonal (T, *P*4*mm*) [9,21], reporting a tricritical point of the R-T phase boundary with the cubic (C, $Pm\bar{3}m$) phase. At room temperature, Haugen *et al.* observed two phases (*R*3*m* and *P*4*mm*) using Rietveld refinement for BCZT50. Within a temperature range of 173–425 K, three phase transition steps between R, R+T, T, and C phases were demonstrated at 177 K, 307 K, and 363 K [21]. In contrast, a more recent BCZT phase diagram was developed that also included an intermediate orthorhombic phase (O, *Amm*2), which was supported by several investigations revealing the possibility of the three phase transitions, *i.e.*, R-O, O-T, and T-C [18,22,23]. After examining the BCZT0–100 range from 80 to 450 K, Keeble *et al.* proposed the existence of an intermediate orthorhombic phase (*Amm*2) between rhombohedral and tetragonal [18]. The intermediate phase was observed close to room temperature with either R or T phase for BCZT40–50. However, Abdessalem *et al.* suggested the existence of the room temperature three phases, *i.e.*, R+O+T, at the triple point of BCZT phase diagram by using Raman and XRD [20]. Some dielectric measurements also observed this intermediate phase and the phase transition sequence of BCZT30–70 range [10]. The concept of a bridging orthorhombic phase in BCZT has been previous demonstrated by various researchers [18–20]. However, the effect of the cation substitutions on the local structure and its effect on the phase transition shifts and the physical properties remains unclear.

It is understood that this complex phase region is responsible for the observed electromechanical properties, although the origin remains under debate. Recently, however, an electric field induced T to O phase transformation could be observed in $BaTiO_3$ [24]. Similar to previous works on the enhancement of functional properties in the vicinity of the MPB of PZT [25], it is possible that the miniaturization of coexisting R or O nanodomains in a matrix of T-domains could play an important role at the PPB in BCZT [26,27]. The coexistence of nanodomains was suggested to be the reason for elastic and dielectric anomalies with no significant contribution to small signal properties by domain wall motion [23]. Moreover, the flattening of the free energy close to phase boundaries was argued to be the driving mechanism of the large piezoelectric response [9,28,29]. Such disagreements on coexisting phases and transition regions close to the polymorphic boundaries have complicated the understanding of the BCZT system and, subsequently, the resulting properties [22].

In addition to XRD, Raman spectroscopy has also been used to determine the structural modifications and the phase transitions in perovskite-like materials, including the $BaTiO_3$ family [30]. This technique is non-destructive and versatile, allowing measurements with adjusted spatial resolution and under different conditions of temperature, pressure, and electric field, in order to enhance the understanding about chemical bonding and local distortion of BO_6 octahedra, causing different macroscopic responses [30–35]. For example, Buscaglia *et al.* [33] identified the ferroelectric-to-paraelectric transition in $Ba(Zr,Ti)O_3$ compounds by using temperature-dependent Raman spectroscopy. More recently, Coondoo *et al.* [19] reported a detailed temperature-dependent Raman investigation only of a $0.5Ba(Ti_{0.8}Zr_{0.2})O_3$-$0.5(Ba_{0.7}Ca_{0.3})TiO_3$ ceramic, identifying the phase transitions by using the intensity, frequency position and width of the main stretching vibrational mode of the <Ti–O> bond in [TiO_6] octahedra. Nevertheless, the broad vibrational bands associated with the BCZT ceramics will have variations depending on the composition and in turn, on the site occupancy, making it difficult to discriminate modifications of the vibrational modes exclusively associated with symmetry. Therefore, a more detailed study of how the vibrations change depending on temperature and composition is needed.

This study aims to provide a comprehensive understanding of the polymorphic phase boundary (PPB) region and structural evolution of BCZT. The structure of polycrystalline BCZT is discussed in terms of the Ca and Zr substitutions in $BaTiO_3$-based lead-free ferroelectrics. The room-temperature structure was identified as a function of Ca/Zr ratio across the polymorphic phase transition region using high resolution X-ray diffraction (HR-XRD) and the pair distribution function (PDF) from the X-ray total scattering. *In situ* temperature-dependent Raman spectroscopy was used to investigate the effect of Ca and Zr substitutions on the AO_{12} and BO_6 polyhedra as well as the impact of temperature variation on the structure. This study additionally explored how the possible rotation and distortion of the polyhedra causes the phase transitions along the PPB in BCZT. In addition, *in situ* temperature-dependent local structure was characterized with PDF analysis and compared with the temperature-dependent Raman spectroscopy and dielectric response to gain insight into the thermally induced structural transitions and the interatomic interactions observed in BCZT. All observed data are in good agreement, and the local scale variations are consistent with the macroscopic dielectric response. Indeed, the changes in site occupancy that are linked to the occurrence of the polyphase boundaries are correlated with the distortion of the polyhedra.

Table 1
The Ca:Ba and Zr:Ti atomic % ratios as determined by ICP-OES for the compositions under investigation in this study as well as the average grain size (including standard deviation).

Composition	Ca:Ba	Zr:Ti	Average Grain size (μm)
BCZT40	0.125:0.875	0.118:0.882	53±29
BCZT45	0.134:0.866	0.106:0.894	34±13
BCZT50	0.149:0.851	0.096:0.904	24±10
BCZT55	0.162:0.838	0.087:0.913	18±5
BCZT60	0.185:0.815	0.082:0.918	17±5

2. Experimental methodology

Polycrystalline $(1-x)Ba(Zr_{0.2}Ti_{0.8})O_3$-$x(Ba_{0.7}Ca_{0.3})TiO_3$ (BCZT, $x =$ 0.40, 0.45, 0.5, 0.55, and 0.6) samples were synthesized with the conventional solid-state reaction method using high-purity ZrO_2 (99.5%, Sigma Aldrich), $CaCO_3$ (99.0%, Sigma Aldrich), $BaCO_3$ (99.8%, Alfa Aesar), and TiO_2 (99.8%, Sigma Aldrich) as starting powders. The starting powders were stoichiometrically weighed in a glove box (relative humidity <10%), mixed, and subsequently ball-milled for 24 h in ethanol absolute with zirconia milling balls (5 mm). Following this, the powder was dried in a rotary evaporator and calcined for 3 h at 1300 °C. One-step sintering was carried out for 4 h in air at 1500 °C with heating/cooling rate of 5 K/min. Details of the ceramic processing can be found elsewhere [13]. For clarity, samples are labelled based on the BCT content, *i.e.,* BCZT*x* with $x = 40$, 45, 50, 55 and 60 mol%.

The microstructure was analyzed using a scanning electron

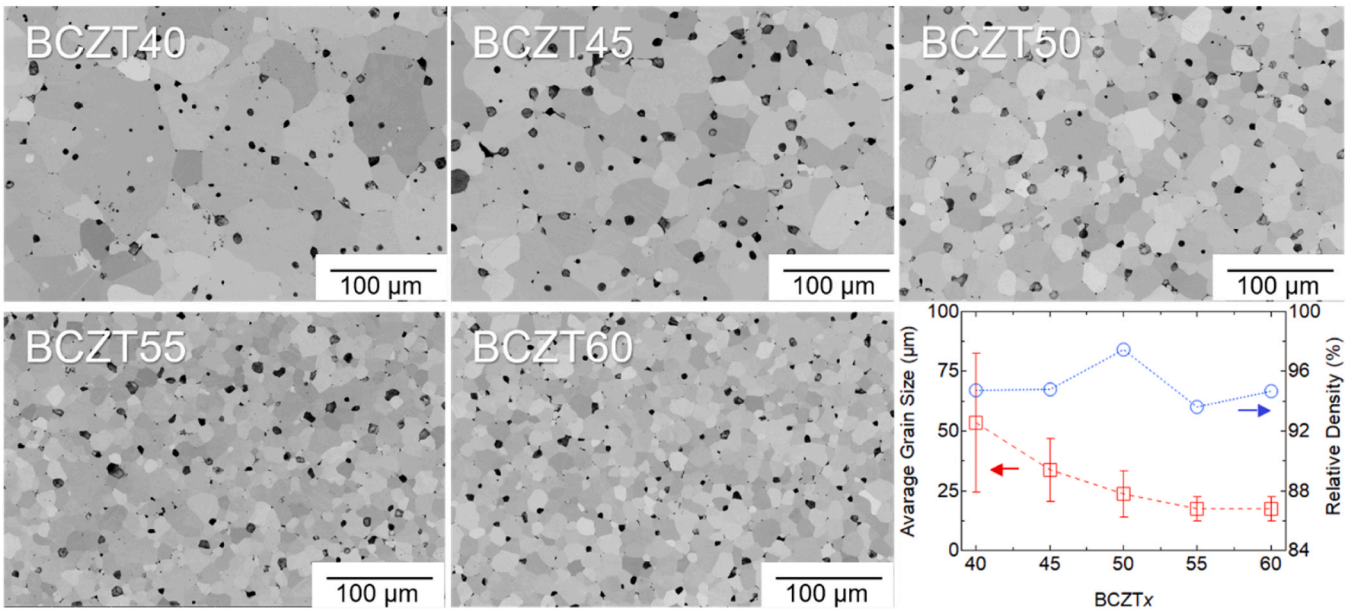

Fig. 1. SEM images of the microstructure of the BCZT*x* samples. The average grain size (red squares) and relative density (blue circles) are reported.

microscope (SEM, Helios NanoLab 600i FIB Workstation, FEI Company, Oregon, USA). The respective samples were polished with a 1 μm diamond suspension, followed by a final treatment with an oxide-polishing suspension (0.05 μm), which was found to be sufficient to observe the grain boundaries. Grain size analysis was performed using ImageJ software [36] on three images of respective samples where at least 100 grains were measured per image. The chemical analysis of the samples was performed using inductively coupled plasma optical emission spectroscopy (ICP-OES, Spectro Genesis, Spectro Analytical Instruments GmbH, Germany). The results show a good agreement between nominal and experimental compositions (Table 1). Archimedes' method was used to determine the density of the sintered samples. The weighing was performed on three samples for each composition.

The phase fractions of powder samples were determined at room temperature using high-resolution powder X-ray diffraction measured at the beamline P02.1 at PETRA III (DESY Hamburg, Germany) with a Perkin Elmer 2D detector (XRD 1621 N ES) using monochromatic radiation with a wavelength of 0.20703 Å [37]. Full pattern structural refinements of all the diffraction data were conducted using the software package TOPAS v.5 [38]. LaB_6 was used to optimize the instrumental peak shapes for XRD data using Pseudo-Voigt function in TOPAS. The background was fitted with Chebychev polynomial function. Beyond that, phase-specific peak broadening parameters were refined to account for crystallite size and microstrain effects. Rietveld refinement was used for the lattice parameters and atomic positions, whereas the A-site atoms were kept fixed at the original position (0, 0, 0) in all refinements [39,40]. The site occupancy was determined after ICP-OES data.

The variation in the local structures as a function of composition and temperature was investigated by PDF. The samples were sealed by a Kapton® film during the measurements. X-ray total scattering measurements were carried out at 25–130 °C on the high-energy X-ray diffraction beamline, BL04B2 at SPring-8 (Japan). For the measurement, the powder sample was sealed in a silica glass capillary (inner diameter of 2 mm) using a Torr-seal®. Samples were irradiated with a monochromatic X-ray beam with the incident energy of 61.2 keV (λ = 0.2025 Å), and the scattered X-rays were detected by seven-point-type detectors. The obtained Q range for PDF analysis, was more than 20 $Å^{-1}$. The structure factor $S(Q)$ was calculated by normalizing the scattering intensity by the atomic number density and the scattering factor of the constituent atoms. The reduced pair distribution function (PDF), $G(r)$, $T(r)$ was obtained by the inverse-Fourier transform of $S(Q)$.

Sintered ceramics cylinders with a height of 6 mm (±0.02 mm), and a diameter of 5.8 mm (±0.02 mm) were ground from a ceramic block with a surface grinder. Following this, the samples were annealed at 600 °C to depolarize the materials and remove any domain state that might have been induced during preparation. All samples were sputtered with platinum electrodes for dielectric measurements on the parallel cylindrical faces (~70 nm). A custom-built thermal chamber equipped with an LCR meter (E4980AL, Keysight, USA) was used to characterize the dielectric measurements from −50 °C to 150 °C with a heating rate of 2 K/min. Liquid N_2 was used to cool the samples down to −50 °C. Permittivity data were collected in a temperature-resolved mode, *i.e.*, at each 0.5 °C step.

Raman spectra of the five samples were acquired by using a coherent Sapphire single-frequency 488 nm laser (output power 100 mW) as the excitation source, an iHR 320 Horiba monochromator coupled with a Syncerity UV–VIS CCD camera, and a custom-built optical microscope. The 1800 lines/mm holographic grating and a long working distance 50× microscope objective (OptoSigma PAL-50-L, NA 0.42) provided spatial and frequency resolution of ~1 μm and ~2 cm^{-1}, respectively. The laser is circular polarised on the sample, making the signal not sensitive to the crystallographic orientation effect. Raman data were first collected at room temperature. Since the grain size of the sintered samples varies from ~20–50 μm (see Section 3.1), an average of 3–6 Raman spectra were collected randomly to observe possible variations due to crystallographic orientations. Temperature-dependent spectra were collected in the range from −65 °C to +130 °C in the combined Raman-DSC (PerkinElmer DSC 8500) experimental set-up with a 2 K/min constant heating rate, to resemble the dielectric data collection. The setup is described in detail in Veber *et al.* 2018 [41], along with the temperature stability of the DSC and the influence of the laser radiation on the sample temperature. The acquisition parameters of the Raman spectra were selected in order to follow the 2 K/min heating rate, with two acquisitions of 28 seconds for each spectrum.

Data reduction was performed using the LabSpec® software (Horiba Jobin Yvon). Raman data collected at room temperature in the frequency range 40–1550 cm^{-1} were background-subtracted with a linear function and normalized to the total area. The temperature-dependent Raman data were acquired in the frequency range 50–1560 cm^{-1} and as well background-subtracted with a linear function and normalized to the total area in the 100–900 cm^{-1} range. Comparing Raman spectra collected at different temperatures would require the removal of the

contributions from thermally populated excited vibrational states. This could be done by applying the Bose-Einstein distribution. However, it causes drastic dumping of the vibrations below 300 cm^{-1}. Therefore, to better visualize all contributions to the spectra, we show the temperature uncorrected Raman spectra and we preferred to use the relative intensity (intensity ratio) of the vibrational modes to identify possible structural changes at different temperatures. The identification of the phase transition regions, and of the structural variations occurring depending on the A-, B- sites substitutions have been carried out with several procedures:

i. frequency, intensity, or width of a particular vibration as a function of temperature/composition, *e.g.,* [19];
ii. curve fitting (or spectral deconvolution) with mathematical functions, *e.g.,* [19];
iii. the barycenter of a specific frequency region (or center of mass), which is used to determine the shift or sudden intensity variations of broad bands [42];
iv. the intensity ratio between main frequency regions, *e.g.,* [33].

For the latter approach, the data analysis was carried out by using Spectral Profile and Map Analysis functions available in LabSpec® that allows calculating the average intensity in a region of interest (ROI) when analyzing spectral arrays and determining the ratio of average intensities in two different ROIs. The data analysis of the Raman signals was carried out also by using the derivative spectra. Indeed, derivatives can help resolve peak overlap and eliminate constant and linear baseline drift between samples or for different acquisition temperatures [43]. To avoid modifications of the bands, we selected the appropriate moving window size for each dataset, and while the polynomial order was kept constant (2), the moving window size of the Savitzky-Golay filtering was varied from 15 to 45 (for particularly noisy signals).

3. Results and discussions

3.1. Composition and microstructure

The microstructure and density of BCZT as a function of composition was characterized (Fig. 1), where the average grain size was found to decrease with increasing the BCT/BZT ratio. The largest and smallest average grain size was observed in BCZT40 and BCZT60, respectively, with values of 53 μm (standard deviation of ±29 μm) and 17 μm (±5 μm). As shown in Fig. 1, the grain size distribution was inhomogeneous for BCZT40 compared to BCZT60. In addition, the relative density for all compositions was 94–97%, in agreement with previous studies [10,44]. Interestingly, the decrease in the grain size can be correlated to substituting large atoms with smaller ones, *e.g.*, substitute Ba with Ca on the A-site, whereas in the B-site, Ti substitutes Zr [44]. Additionally, it is known that the doping of Ca in $BaTiO_3$ suppresses abnormal grain growth, which partially explains the decreasing grain size [45]. Nevertheless, the surface diffusion also directly contribute to BCZT grain growth [46,47].

The increase of Zr content over Ti in the B-site is combined with the shifting of the oxygen in the [BO_6] octahedron due to the larger ionic radius of Zr over Ti, *i.e.*, 0.72 Å and 0.605 Å, respectively, [48], which leads to higher internal chemical pressure in the unit cell. Interestingly, the increase in grain size with higher Zr content can be related to a surface diffusion enhancement. These phenomena also can explain the existence of enclosed pores within large grains. Whereas for small grains, the pores are located mostly along the grain boundaries. Similar effects were shown for Bi-deficient (Na,Bi)TiO_3, where the depletion of Bi causes an increase in the oxygen vacancies and consequently enhances surface diffusion [49–51]. Moreover, in the case of $BaTiO_3$, pores at grain boundaries may move with the boundaries during sintering and eventually coalesce at higher sintering temperatures [52]. In contrast, intragranular pores could be obtained due to some impurities and

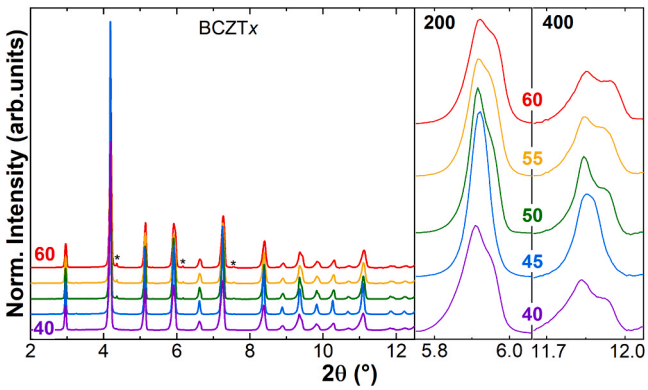

Fig. 2. High-resolution XRD data of BCZT*x* powders, where $x = 40$, 45, 50, 55, and 60. A magnification of the 200 and 400 reflections is reported on the right panels. * represents the minor secondary phases ($CaTiO_3$).

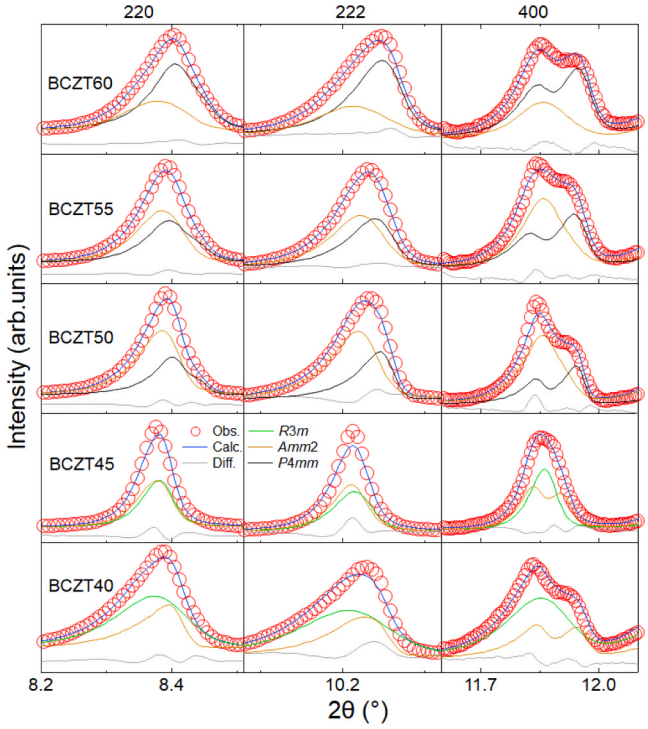

Fig. 3. Observed, calculated, and difference curves from the Rietveld refinement of pseudo-cubic 220, 222, and 400 reflections at room temperature with different phases, *i.e.*, *R*3*m*, *Amm*2, and *P*4*mm*, of BCZT powders.

defects in the starting powders as well as grain growth [53,54]. The chemical composition of the different samples was determined by ICP-OES, and the Ca:Ba and Zr:Ti atomic ratios for BCZT*x* are reported in Table 1. The results show a good agreement between nominal and experimental compositions.

3.2. Crystal structure

3.2.1. X-ray diffraction as a function of composition at room temperature

High-resolution X-ray powder diffraction data for all compositions were collected at room temperature (Fig. 2). The resulting diffraction patterns showed a BCZT perovskite structure with a possibility of minor secondary phases ($CaTiO_3$) within the resolution of the measurements. Based on the $BaTiO_3$ (BTO) structure, the A-site cations Ba (1.61 Å) was substituted with Ca (1.34 Å) and Ti (0.605 Å) with Zr (0.72 Å) on the B-site [48]. A decrease of the *d*-spacing with increasing BCT/BZT molar

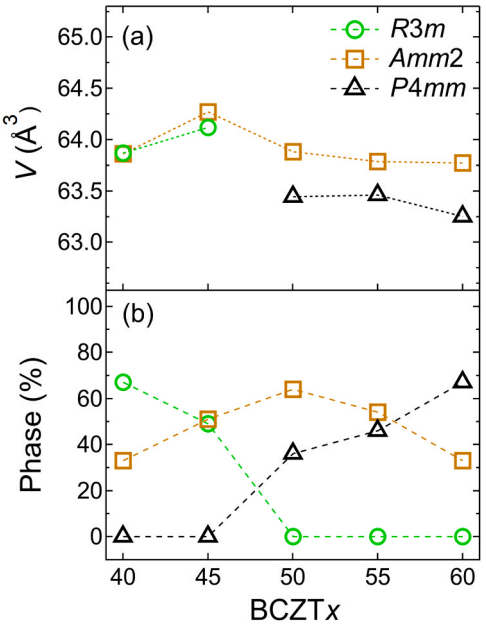

Fig. 4. Unit cell volume (a) and phase fractions (b) as a function of BCT content in BCZT. Orthorhombic supercell volume was divided by 2. Error bars are within the symbols.

ratio was observed due to the different ionic radii of Ba and Ca. Furthermore, the change in the composition affected the peak shape and symmetry. As shown in Fig. 2, the splitting of the 200 and 400 reflections demonstrates the change in symmetry from rhombohedral to tetragonal [18,23], and by increasing the BCT/BZT ratio the samples presented increased tetragonality. However, at BCZT45, the reflections appear more symmetric and exhibit less splitting, which can be related to the phase instability region at room temperature for BCZT45, as reported in the previous BCZT phase diagram [10,18].

Rietveld refinement was performed to determine the crystal structure of BCZT*x* powder samples as a function of composition (Fig. 3). In this study, the crystal structures were refined after Keeble *et al.* [18] with structure models of coexisting phases, *i.e.* rhombohedral R, orthorhombic O, and tetragonal T. At room temperature, BCZT45, 50, and 55 powders are in the vicinity of the polymorphic phase boundary consisting of R and T phases, separated by an interleaving O phase. Therefore, coexisting phases of *R*3*m* and *Amm*2 were used during refinement for BCZT40 and 45, whereas BCZT50, 55, and 60 were refined with a mixture of *Amm*2 and *P*4*mm* [10,23,55]. Both BCZT45 and 55 have similar phase fractions of R-O and O-T, respectively. In contrast, BCZT50 showed the highest orthorhombic phase content among the other compositions (Fig. 4b). Detailed refinement results without considering the O phase in BCZT40 and BCZT60 are reported in the Supplementary materials (Figure S1).

The unit cell volume as a function of BCT content is reported in Fig. 4a. With an increasing BCT/BZT content there was an initial increase in the unit cell volume at BCZT45, followed by a subsequent decrease up to BCZT60. The initial increase in rhombohedral unit cell volume was observed to be from 63.9 Å^3 to 64.1 Å^3 and the orthorhombic volume increased from 63.9 Å^3 to 64.3 Å^3 for BCZT40 and 45, respectively. This sudden increase in unit cell volume can be related to the increase in polyhedral distortion in A- and B-sites during the refinement (CIF files available in the Supplemental Materials). For example, in rhombohedral phase, the B–O distance varies between 1.971–2.029 Å for BCZT40, whereas in BCZT45 the B–O distance range is 1.873–2.141 Å. Moreover, the change in elongation of the octahedra causes an expansion in the volume associated with increasing dielectric polarization in BCZT45 [56]. Acosta *et al.*, for example, reported a high d_{33} of BCZT45 at room temperature compared to the other compositions

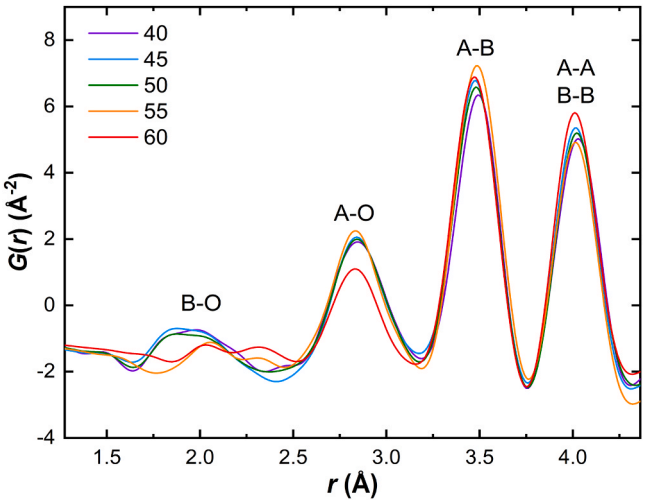

Fig. 5. Room temperature experimental pair distribution functions of BCZT*x* powders (x = 40, 45, 50, 55, 60).

[14], which is likely related to phase instability in BCZT45, as the PPB is located directly at room temperature [11].

The 220, 222, and 400 reflections have been extracted from the previous diffraction data and are shown as a function of composition in Fig. 3. It is apparent that the reflection splitting of 400 and the asymmetry of 220 and 222 indicate a minor orthorhombic phase [18] in BCZT40 and 60 at room temperature. In comparison, a single phase of *R*3*m* for BCZT40 and *P*4*mm* for BCZT60 showed a poor fitting with the observed data (see Figure S1). Thus, a combination of rhombohedral *R*3*m* and orthorhombic *Amm*2 was used for better fitting during refinements and lower GOF values. The obtained phase fractions for BCZT40 were 66:34 for *R*3*m* and *Amm*2, respectively. Also, in BCZT60, the minor orthorhombic *Amm*2 was combined with the tetragonal *P*4*mm* in the refinement, with phase fractions 33–67, respectively (Fig. 4b). The existence of orthorhombic phase in BCZT40–60 powders can be explained due to the relatively low temperature of calcination compared to sintering temperature [10]. Similar results were reported by Keeble *et al.*, where the orthorhombic phase was observed at BCZT40–50 powder samples [18].

3.2.2. PDF analysis as a function of composition and temperature

The room temperature local atomic structure of BCZT was investigated by PDF as a function of composition with synchrotron X-ray total scattering (Fig. 5). The peak positions represent the interatomic distances between the A-site, B-site, and oxygen ions, *i.e.*, A–O, B–O, A–B, A–A, B–B. The resulted PDF pattern of BCZT is similar to the previously observed patterns of BTO, BCT, and BZT [57–59], which follows the perovskite type structure. The first peak at ~1.64–2.3 Å represents the average Ti/Zr–O distances in the B-site, whereas Ca/Ba–O was observed at ~2.6–3 Å [48]. Around 4 Å, both A–A and B–B distances were observed and represent the unit cell lattice constants. The Ca/Ba and Zr/Ti ratios changes in the BCZT systems showed relatively insignificant shifts of the peak positions and change in shape, *i.e.*, A–O, A–B, A–A. For example, the A–A and B–B interatomic distances insignificantly shift to lower values with increasing Ca and decreasing Zr, which matches well with the unit cell volume change from XRD data. On the contrary, the B–O bond showed a significant change in the shape and position, depending on the BCT/BZT ratio. The B–O peak is broad and shows strong variations when changing the Zr/Ti ratio. The broad peak spans from ~1.65–2.34 Å and peaks at ~1.99 Å in BCZT40 to BCZT50, and these interatomic distances match well the one determined by XRD. The PDF patterns of the B–O site drastically change in BCZT55 and 60, with the whole peak shifting toward longer distances and showing two maxima, respectively at ~2.14 Å and 2.34 Å. The XRD data refinement

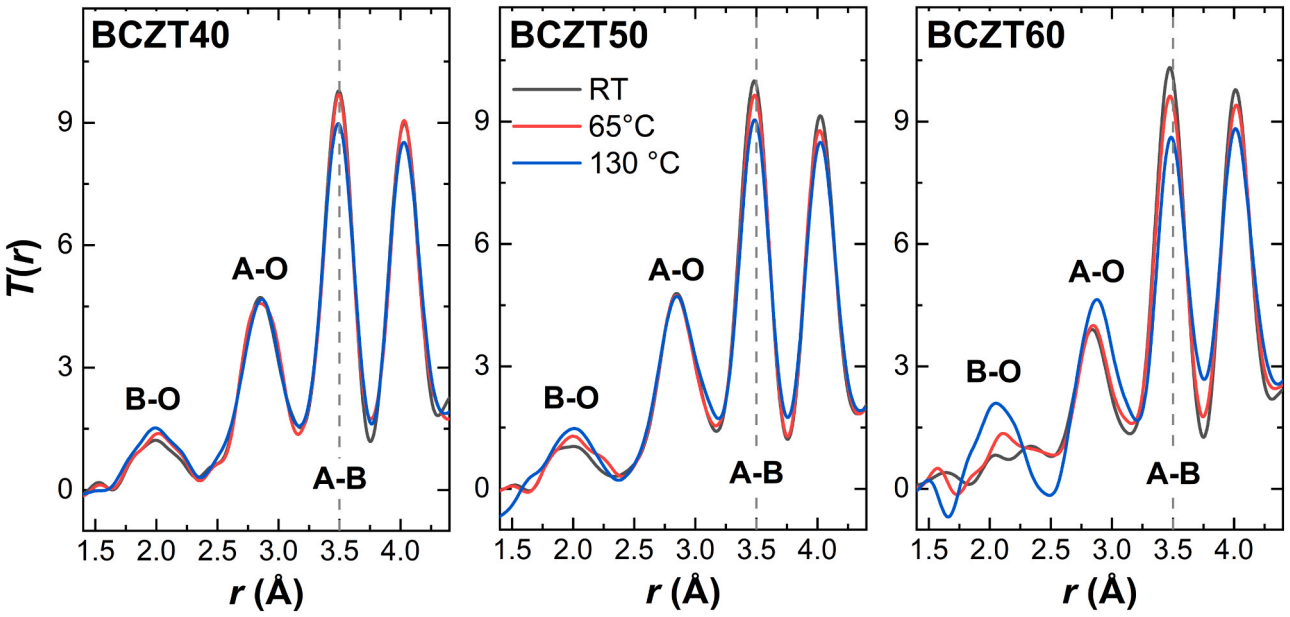

Fig. 6. Temperature dependent experimental pair distribution functions of BCZT*x* powders (x = 40, 50, 60). The samples were measured at RT, 65 °C, and 130 °C.

of these two compositions recorded the occurrence of orthorhombic and tetragonal phase with B–O distances between 1.83–2.18 Å. The occurrence of longer interatomic distances in the PDF patterns of BCZT55 and 60 could have different origins: i) an anomaly due to the *cut-off* of the Fourier-Transform [60,61]; ii) the increase in tetragonality in BCZT55 and 60 that could lead to an increase in the distance between B-site cations and oxygen, similarly to what observed by Culbertson *et al.* in Zr–O nPDF peak (2.15 Å) and by EXAFS spectroscopy (2.0–2.19 Å) due to *P4mm* symmetry with lower octahedra distortion [62]; iii) Ca cations entering the B-site, which would cause longer distance (<Ca–O> in a 6-fold coordinated environment ~2.35 Å) as already reported by [63]; and iv) Ca–O bonds (2.25–3.0 Å) from the observed secondary phase $CaTiO_3$ by XRD (see Fig. 2), which is similar to the previously reported by nPDF study of $CaTiO_3$ [64]. One could speculate that the broad B–O peak in the PDF pattern consists of three contributions, whose relative intensity seems to match the phase content estimated by XRD. The PDF data does not allow to distinguish between the Ti–O and Zr–O contributions, and further detailed investigation, such as neutron diffraction, must be done.

Furthermore, temperature-dependent pair distribution functions of BCZT40, 50, and 60 were measured at 65 °C and 130 °C to study the effect of the crystal symmetry on the atomic distances (Fig. 6), where all samples are tetragonal at 65 °C and cubic at 130 °C. Although all peak positions were shifted to higher values due to thermal oscillation, in the case of B–O, the peak shape and position changes arbitrary with increasing temperature. For example, at 65 °C, the peak shifts to higher value for BCZT40 and 50, but not for BCZT60. This can be related to the change in the crystal symmetry to tetragonal in the case of BCZT40 and 50 after crossing the O-T phase transition, whereas in the case of BCZT60 no change in the crystal symmetry was observed. The peak shape and shifting are reciprocally dependent on the Zr/Ti content in the B-site. Interestingly, at 130 °C, B–O peak showed low splitting with shifting to lower value for all samples. This can be related to the crystal symmetry of all samples turned into cubic after crossing the T-C phase boundary. This effect has been also reported for BCZT50 nPDF (neutron pair distribution function) analysis, where the Zr–O distance decreased from 2.19 Å to 2.09 Å for *P4mm* and $Pm\bar{3}m$, respectively [62].

Moreover, the increase of smaller cations, *i.e.,* Ca and Ti, and the decrease of Ba and Zr contents in the unit cell leads to more free space within the unit cell, even if the overall volume of the cell does not significantly change. That gives more degrees of freedom to the interatomic angles' variations and, subsequently, to the distortion of the octahedra cage by shifting the oxygen ions further toward the A-site. By increasing the Ca/Ba content, the A-site presents shorter <Ca–O> distances, causing disorder (*e.g.*, octahedra elongation) in B–O bonds, even if both the A- and B-site cations remain in fixed positions. Therefore, in the case of BCZT60, the interatomic bonds showed significant variations with temperature as it has smaller cations and more free space within the unit cell. In contrast, BCZT40, which has larger cations causing high compaction within the unit cell and less degrees of freedom, displayed insignificant changes in the interatomic bonds. Previous studies have reported the similar interplay between A and B-site in perovskites and its relation to the phase stability and coexistence of different phases [65,66]. The observations regarding the small variations in the interaction between the ions in the case of BCZT40 can explain the diffuse phase transitions and phase coexistence in the dielectric data and piezoelectric coefficient [67]. Indeed, the limited variations in the Jahn-Teller distortions as well as the octahedral rotation, clarify the continuous evolution of the symmetry in a narrow temperature range.

3.2.3. *Raman spectroscopy at room temperature: influence of chemical composition on PPB*

Raman spectra collected at room temperature in the frequency range 20–1400 cm^{-1} are shown in Fig. 7. The five samples show relatively broad vibrations representing stretching of the <Ti–O> bond in [TiO_6] octahedra as well as bending modes of the Ti–O–Ti bonds. At low frequencies (~100 cm^{-1}), there are vibrations of the A-site cations against the [BO_6]-octahedra. The main discernible Raman vibrations are transverse (TO) and longitudinal (LO) modes peaking at ~110, 150, 190, 235, 293, 470, 520, 720, and 800 cm^{-1}. For clarity, we will divide the spectra into three main regions: the low-frequency region (LF) from 90 to ~350 cm^{-1}, the intermediate frequency region (IF, between ~440–650 cm^{-1}, and the high frequency (HF) region from ~680 to ~900 cm^{-1}. Each of these regions has main vibrations, highlighted in Fig. 7, and based on literature data, a list of assignments of the Raman bands in perovskite-type structures is reported in Table 2 ([19], and references therein).

The frequency shift, sudden intensity variations, disappearance, and appearance of some Raman vibrations could be used to determine the phase transition regions. In general, this is done by considering frequency, intensity, or width of a particular vibration as a function of composition. Depending on the perovskite crystal structure, a few bands

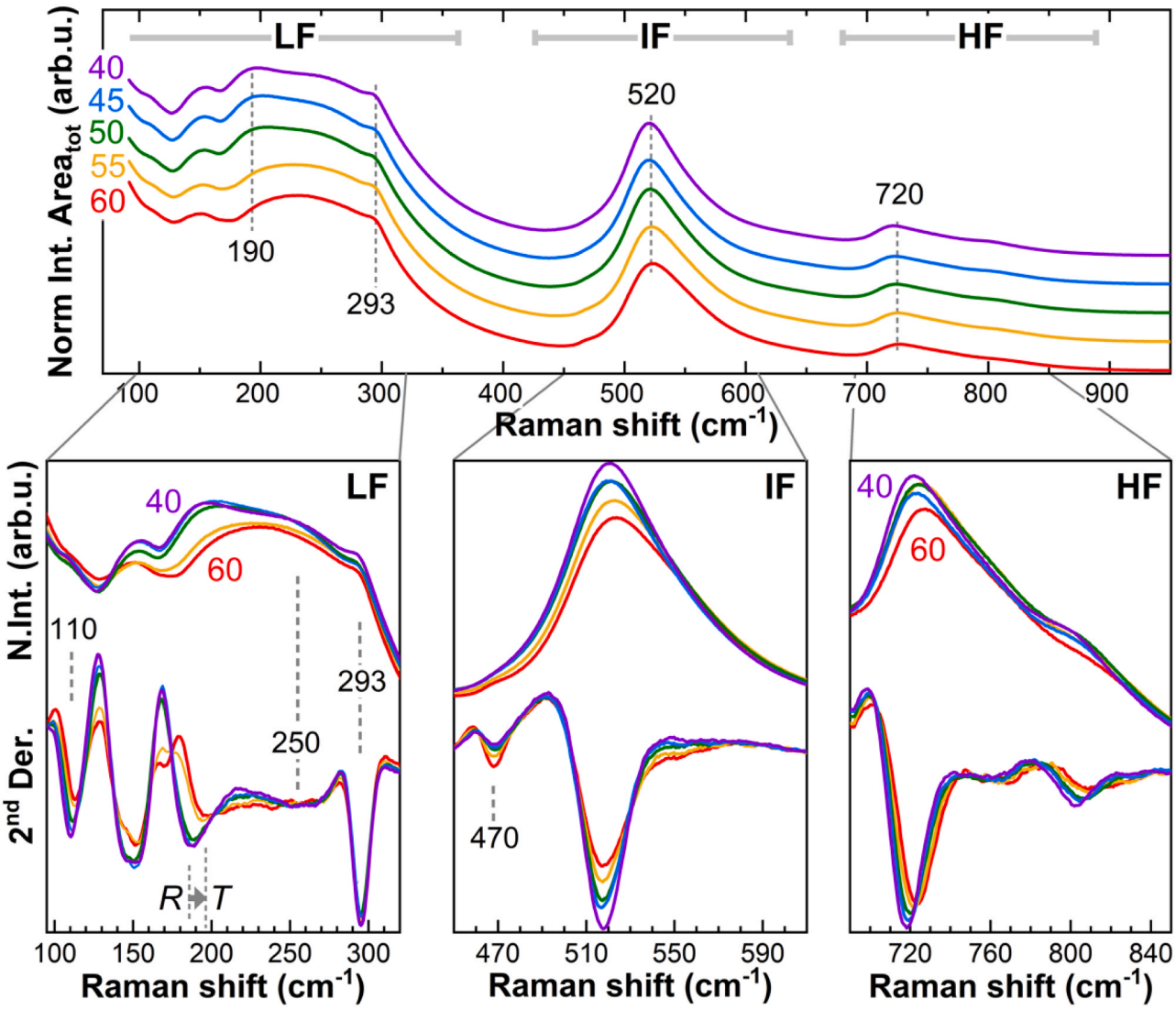

Fig. 7. Normalized room temperature Raman spectra of BCZTx (x = 40, 45, 50, 55, and 60 mol%). The spectra are divided into three main frequency regions: low (LF), intermediate (IF), and high (HF) frequency. A magnification of each region, together with the second derivative of the signals, is depicted in the lower panels. HF and IF regions show systematic shifts of the main vibrations associated with the site occupancy. The LF region shows stronger changes, with the ~190 cm^{-1} band being a fingerprint of structural variations between R and T phases.

Table 2
Approximate position of the transverse (TO) and longitudinal (LO) modes in the BCZTx samples. Band assignments in perovskite-type structures are done according to literature ([19], and references therein).

Region	Raman Band Position	Mode
Low-frequency (LF)	110	A_1 (TO_1)
	152	E (TO_2)
	195	A_1 (LO_1)
	240	A_1 (TO_2)
	293	B_1 E (LO_2)
Intermediate frequency (IF)	470	E (LO_3) A_1 (LO_2)
	520	A_1 (TO_3)
High frequency (HF)	722	E (LO_4) A_1 (LO_3)
	803	A_{1g}

have been previously used as fingerprints for symmetry identification, such as the vibrational modes ~110 cm^{-1} in the frequency range below 200 cm^{-1}, indicating the presence of the rhombohedral phase [68]. The suppression of these vibrations at low frequencies and the presence of a relatively sharper mode at ~293 cm^{-1}, together with a small contribution at ~470 cm^{-1}, have been associated with the stabilization of tetragonal and orthorhombic phases. The change from a ferroelectric to a paraelectric phase has been related to the disappearance of the mode at ~293 cm^{-1} and the drastic suppression of the ~720 cm^{-1} band. The latter is particularly sensitive to the T-C transition [33], and recently, it was shown that the barycenter of the whole band in the HF region could be used to discern this transition [67].

The vibrational modes of the BCZTx samples are broad and mainly overlap. Therefore, the second derivative spectra of the three main frequency regions were used to highlight the variations of the main Raman modes depending on the composition:

i. In the LF region, there is a net difference between samples having higher or lower BCT/BZT ratios and, in turn, different phase symmetries. The main vibration at ~193 cm^{-1} is clearly shifted toward higher frequencies and broader when in tetragonal symmetry (BCZT55 and BCZT60). This is because as the Ca ions are incorporated, the structure becomes more symmetric into a predominantly tetragonal phase with the 55 and 60 mol% BCT content. The contribution at ~250 cm^{-1} is clear only in BCZT40, the sample having the lowest BCT content. On the contrary, the

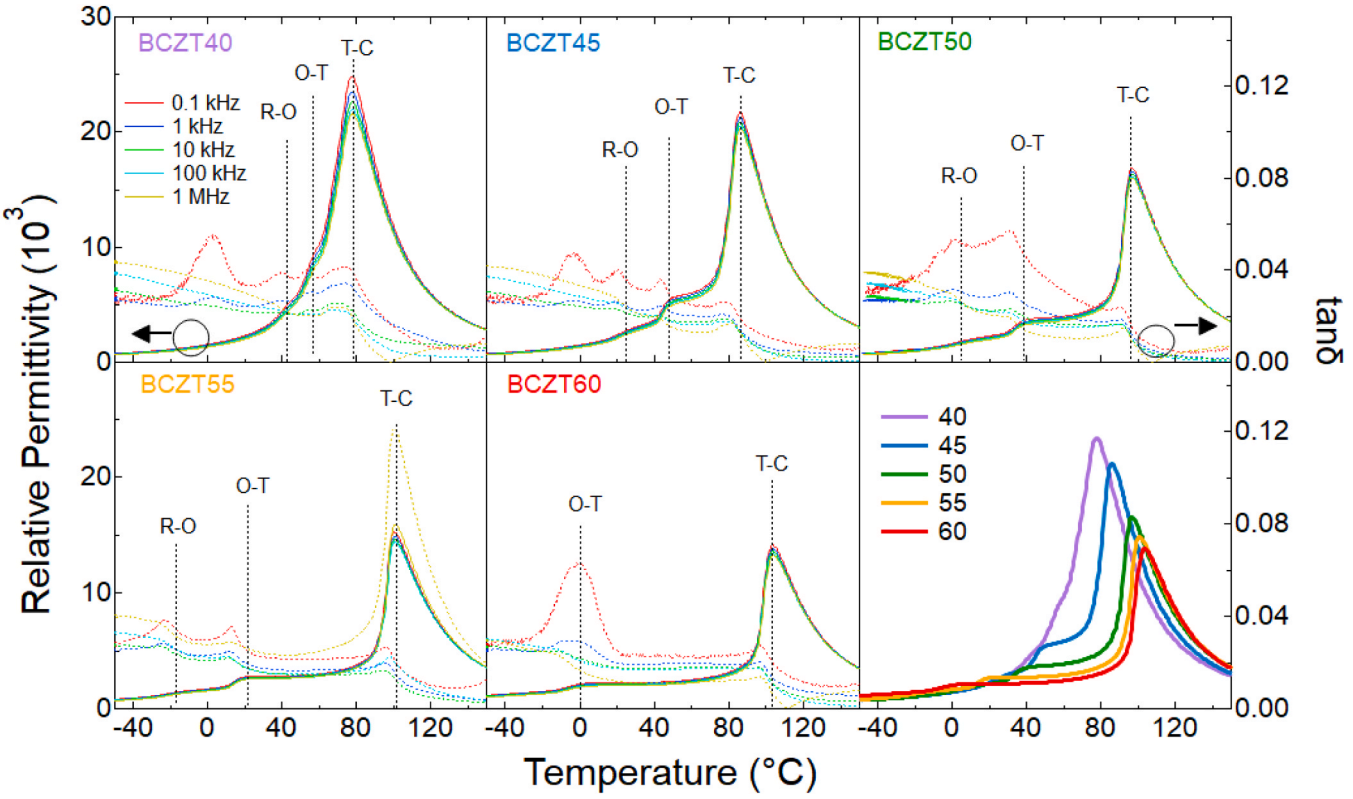

Fig. 8. Temperature-dependent dielectric permittivity (solid lines) and tan δ (dot lines) from −50 °C to 150 °C as a function of BCT/BZT content in BCZT*x* (For compositional comparison, 1 kHz was used for illustration).

mode at ~293 cm^{-1} is sharp and shows almost no differences in all samples but only a slight decrease with BCT content.

ii. In the IF region, there are two contributions: the main one around 520 cm^{-1}, and a small band at ~470 cm^{-1}. The band position estimated around 470 cm^{-1} develops with the increase of xBCT content, which can be seen more clearly from the second derivative (Fig. 7). A small additional contribution is observed at ~550 cm^{-1} for samples having tetragonal symmetry (BCZT55 and BCZT60). The relative intensity of the main mode around 520 cm^{-1} decreases by increasing the BCT/BZT ratio, however, overall, no sudden modifications are observed in the IF region due to the coexistence of tetragonal and lower symmetric phases at room temperature.

iii. The HF region has the main contribution peaking around 720 cm^{-1}, and a second broad band at ~800 cm^{-1}. The most obvious variation is the frequency shift of the main band that linearly moves toward higher frequencies by increasing the BCT/BZT ratio.

The XRD analysis showed phase coexistence within the compositional range investigated here. Therefore, assigning specific Raman vibrations to one or another symmetry is challenging. All changes observed in the IF and HF vibrations seem to be related to the composition; accordingly, these frequency regions are particularly appealing for site occupancy discrimination. To verify the link between the shift of the vibrations and symmetry/site occupancy, we analyzed the frequency, relative intensity, and width of specific vibrations (see also Supplementary materials, Figure S2). The strongest changes observable by increasing the BCT content are the frequency position of the main vibration around 520 cm^{-1} and the width (FWHM) of the whole band in the IF region. Both increase linearly, confirming that the variations are mainly related to the site occupancy rather than symmetry changes. The small vibration at 470 cm^{-1}, usually considered a marker of the stabilization of tetragonal and orthorhombic phases, increases its relative intensity, but without providing a clear trend. Indeed, the intensity ratio between the two main bands within the IF region (I_{520}/I_{470}) decreases, but not in a linear fashion (Figure S2). In the high frequency region, the main contribution decreases its intensity and moves toward higher frequencies by increasing the BCT content; however, the intensity ratio of the two main peaks (I_{720} /I_{800}), previously used as a marker for phase transitions [33] does not provide clear trends with the BCT content. The barycenter of the whole HF region moves as well toward higher frequencies (Figure S2) and highlights the presence of two trends that seem to match the occurrence of higher contents of the tetragonal phase at higher BCT contents, and in turn, the higher bond strength and the smaller mass of Ti substituting for Zr in the B-site. Similar considerations can be done when looking at the barycenter of the IF region (see Section 3.3).

The linear trends found from the study of the vibrations in the IF and HF regions can be used to determine site occupancy in BCZT systems. However, common fingerprints previously used to distinguish the different symmetries, such as the band at ~110, 293 and 470 cm^{-1}, as well as the intensity ratio (I_{720} /I_{800}) do not show any clear trend. In the BCZT samples investigated at room temperature, the Raman vibration that mostly seems to record the change in symmetry (R to T) is the mode at ~193 cm^{-1}. This would agree with the pair distribution functions results that show almost no variations in the interatomic distances between the A- and B-site, but only in the B–O correlation, linked to the octahedra tilt and rotation. Therefore, the symmetry change is mostly marked by the variations in the bending mode at ~193 cm^{-1} in the Raman spectra.

A further attempt to study the different vibrations was done by using the curve fitting (or spectral deconvolution) with mathematical functions. This latter method, used recently by Coondoo *et al.* [19] has shown the ability to detect phase transitions in BCZT50 bulk ceramic. It is a rather time-consuming method that requires assumptions on the

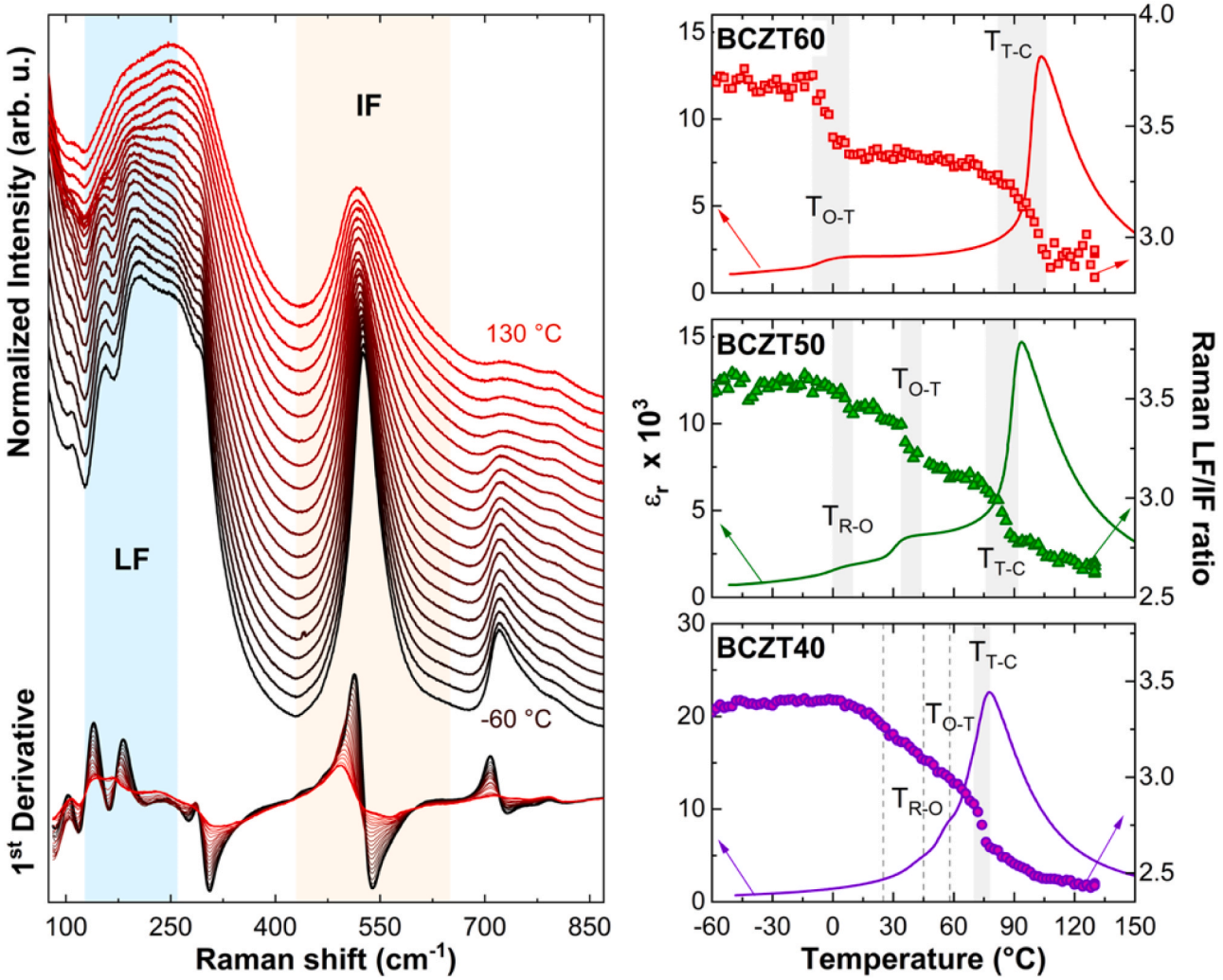

Fig. 9. Left panel: Raman spectra of sample BCZT40 collected at different temperatures from −60 °C to +130 °C (depicted spectra here are collected each 10 °C). The two regions of interest in the LF and IF ranges are highlighted, and the first derivative is shown on the bottom. The right panels show the ratios of the integrated intensities of the two frequency regions (Raman LF/IF ratio, symbols) and the permittivity curves (solid lines) against the temperature. The Raman LF/IF ratios show sudden steps that well correlate with the phase transitions. Shadow areas and vertical dashed lines highlight the sudden steps in the intensity ratios.

behavior of the different vibrational modes, including the number of vibrations, band position, and broadening. To minimize the error, the number of the Gaussian functions and their frequency position were determined from the second derivative of the spectra (see Figures S3 and S4).

In the low-frequency region, the largest variations associated with symmetry changes are the sudden shift toward higher frequencies of the ~190 cm^{-1} and the ~250 cm^{-1} band (respectively, G3 and G4 in Figure S5). Similarly, the smaller contribution in the HF region (band G13 around 800 cm^{-1}) shows this step-like behavior. Consequently, these bands are able to distinguish the transition toward higher tetragonal contents. Despite the different symmetries, all the other vibrationsshow a constant behavior with increasing BCT content, or a linear shift (as in the case of the main bands in the IF and HF regions), or the modes at 110 and at 293 cm^{-1}, which do not show abrupt variations ascribable to the transition between rhombohedral and tetragonal symmetry. Therefore, the progressive shift is mostly related to the site occupancy, and in turn, to variations in bond strength/distances, as already observed in Fig. 7 (and Figure S2). Consequently, the results of the curve fitting are consistent with those obtained by using the second derivative, or the barycenter of the frequency regions: the modes at ~190 cm^{-1}, and ~250 cm^{-1} are the only vibrations related to the symmetry transition to tetragonal.

3.3. Temperature dependent phase boundaries

3.3.1. Temperature-dependent dielectric response

The dielectric permittivity (ε_r) and dielectric loss (tanδ) were measured for unpoled BCZT samples from −50 °C to 150 °C (Fig. 8). These data show dielectric anomalies associated with peaks in the loss curve during heating that are understood to be due to structural phase transitions between R, O, T, and C phases in BCZT [10]. Extra loss peaks are observed for BCZT40 and 45 close to 0 °C at lower frequencies due to water condensation, which are not observed at higher frequencies. With an increasing BCT content there is a corresponding increase in the Curie Point separating the T and C phases [6,10,55] as well as a decrease in both the $T_{R\text{-}O}$ and the $T_{O\text{-}T}$ phase transition temperatures, corresponding well to previous investigations [10,67]. This results in a stabilization of the tetragonal phase with increasing BCT content, as also observed with XRD (Fig. 4). By increasing the BCT content, the T_c values were approximately 77, 86, 93, 98, and 104 °C for BCZT, 40,45, 45, 50, 55, and 60, respectively. In contrast, the R-O transition temperature is shifted from 43 °C to −44 °C and the O-T transition temperature from 56 °C to 0 °C for BCZT40 and 60, respectively. This shift in the phase transition is directly related to the rise of the BCT/BZT ratio. Upon replacing Ti^{4+} cations with relatively bigger cations like Zr^{4+} on the B-site causes an increase in the internal chemical pressure in the

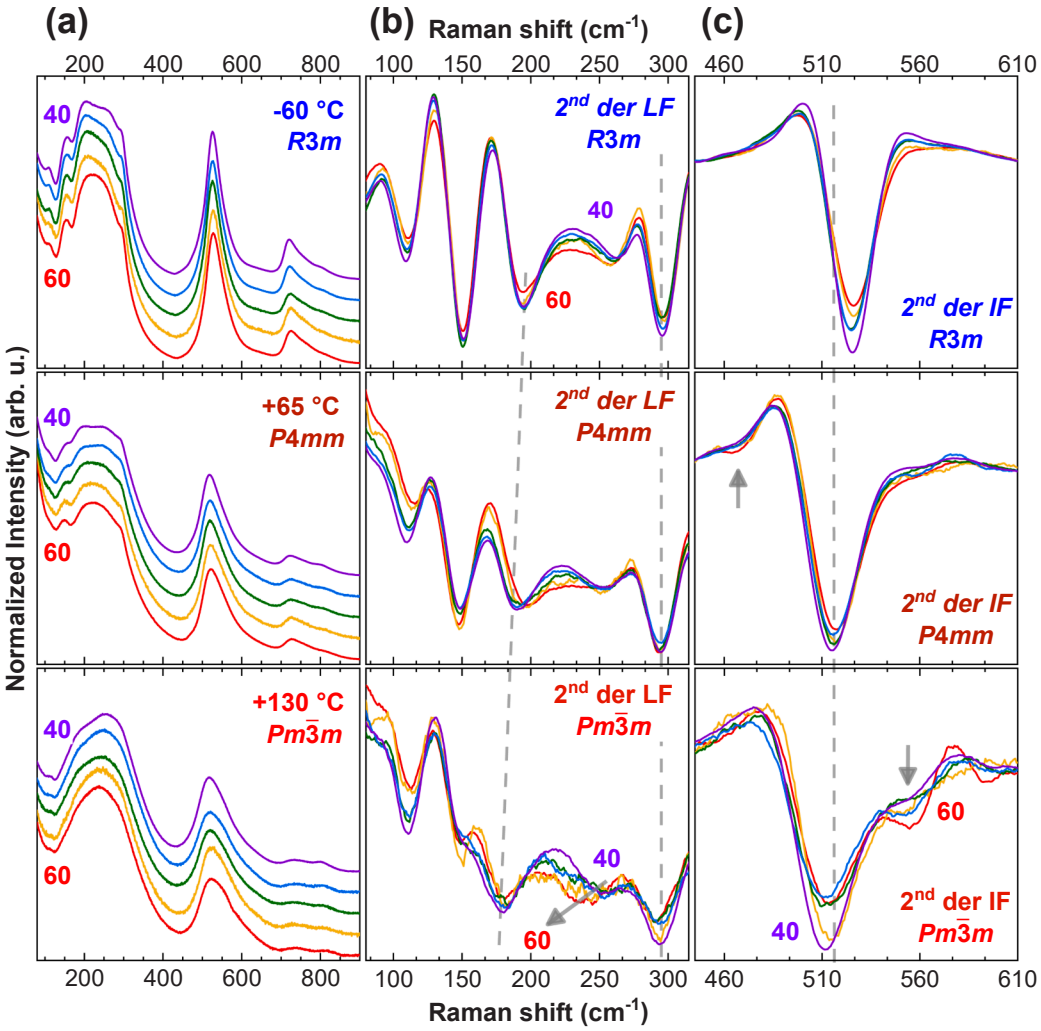

Fig. 10. a) Raman spectra in the frequency range 80–900 cm^{-1} of the BCZT*x* samples (x = 40, 45, 50, 55, 60) collected at equal temperatures (−60 °C, 65°C, and 130°C), corresponding to the stability field of different symmetries. b) Second derivative of the spectra in the LF region and c) in the IF region. The grey arrows highlight the major changes.

octahedra and, accordingly, lower phase stability [69–71]. It is also important to note that the grain size and stoichiometry significantly impact the dielectric properties of perovskite ferroelectrics [72]. The maximum value of dielectric permittivity is a consequence of the BCT/BZT content as well as the grain size. For example, the ε_r maximum values are dropped dramatically from 23447 to 13603 for BCZT40 and 60, respectively. Such a trend has been reported before by Bai *et al.* 2015 [10].

3.3.2. *Temperature-Dependent Raman spectroscopy*

In order to investigate the temperature induced structural phase transitions observed during dielectric measurements, Raman spectra were collected from −60 °C and 130 °C for all BCZT compositions (Figure S6). At the lowest temperature, all samples should have rhombohedral symmetry and the spectra should have much sharper features, whereas at the highest temperature, where all samples are in the paraelectric phase, the bands are weaker and broader. Considering the dependence in temperature, the spectra show an apparent continuous change with a general broadening of the vibrations and a similar evolution from low to high temperatures, regardless of the composition.

Based on the data analysis of the room temperature data, we first identified frequency regions that are more sensitive to structural changes. To avoid any influence of the background (thermal influence) on the intensity, and to simplify the data analysis of temperature-dependent Raman spectra, here we present a simpler approach that considers the derivatives of the spectra and the intensity ratio between the main frequency regions. The data analysis was carried out by using Spectral Profile and Map Analysis functions available in LabSpec® that allows calculating the average intensity in a region of interest (ROI) when analyzing spectral arrays and determining the ratio of average intensities in two different ROIs. For the analysis of the large dataset of *in situ* temperature-dependent Raman spectra, the derivative spectra were first used to determine some vibrations more responsive to structural changes. Second, ROIs were selected in the low and intermediate frequency ranges of the Raman spectra, and finally, the integrated intensity ratio of the two ROIs was calculated for each spectrum. From the first and second derivative spectra of the temperature-dependent datasets, some regions of interest can be highlighted in the low and intermediate frequency ranges: 125–255 cm^{-1} and the 440–650 cm^{-1} range (see Fig. 9, left panel). These frequency portions show changes in the spectra, and when the ratio of the integrated intensity of the two regions (LF/IF ratio) is plotted against temperature, sudden changes in the slope occur. The appearance of discontinuities in the slope of the intensity ratio vs. temperature correlates with structural changes or reordering in the ceramics (Fig. 9, right panels). In particular, BCZT60 has two clear steps: the first between –10°C and 6 °C, and the second one between ~82 °C and 106 °C (see also Figure S7). In the other temperature ranges, the ratio is nearly constant. These two steps agree well with the

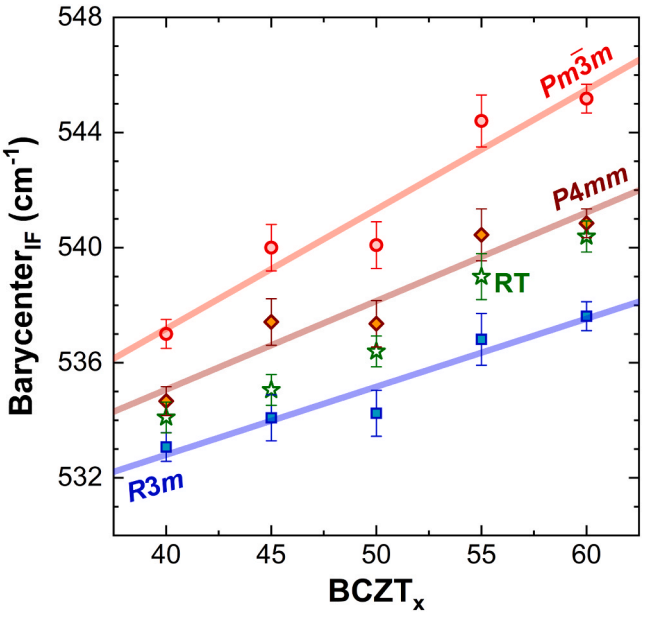

Fig. 11. The barycenter of the IF region evolution depends on the BCZT stoichiometry. Regardless of the symmetry, the whole band moves toward higher frequencies. The phase transition equations are reported in the main text as well as data from the room-temperature (RT) spectra.

temperature-dependent dielectric permittivity and the occurrence of phase transitions. The step at the highest temperature well corresponds to the T_c, and by increasing the Zr content in the B-site, this transition moves toward lower temperatures. Indeed, the steps are in the temperature range ~76–92 °C and ~70–78 °C, respectively for BCZT50 and BCZT40.

BCZT50 shows a step-like curve, with changes in the LF/IF ratio that agree very well with phase transitions identified via permittivity measurements. Indeed, BCZT50 has a step at ~34–42 °C, which matches the T_{T-O} transition measured by permittivity, and another small slope change between 0 °C and +8 °C, corresponding to the T_{O-R} transition (Figure S7). The changes in the LF/IF ratio for sample BCZT40 are more diffused, with the exclusion of the clear step associated with T_c (Fig. 9). From low temperature, the first slope change is between 0 and 20°C, and then the LF/IF ratio almost steadily decreases up to T_c at ~70 °C with two small steps (see derivative in Figure S7) at ~45 °C and 58 °C that match, respectively, the T_{O-R} and the T_{T-O} transitions obtained by permittivity. The observed diffuse transitions are consistent with the occurrence of phase transformations in a smaller temperature range, as highlighted by the permittivity measurements, and a continuous evolution of the octahedral sites (rotation) as highlighted by the PDF results. The data in Fig. 9 show that the ratio of the integrated intensity of the LF and IF regions versus temperature has discontinuities that correlate well with structural changes or reordering in the different BCZT ceramics, and it is a faster and robust method that can be applied to other BCZT systems or different temperature/pressure conditions.

3.3.3. *Effect of cation substitution on the vibrational modes*

To discriminate changes exclusively due to the different occupancies of the [BO_6]-octahedral units that cause changes in bond length/strength, and angles, and in turn, in the vibration frequencies, we compare spectra of the BCZT*x* ceramics collected at the same temperatures where the stability field allows the occurrence of the same symmetry. The temperatures selected for all compositions are: −60 °C (R), 65 °C (T), and 130 °C (C). This approach allows to discard modifications due to symmetry and temperature. Unfortunately, there is no temperature at which the orthorhombic phase occurs for all compositions.

At the lowest investigated temperature of −60 °C, all samples are assumed to have *R*3*m* symmetry. The Raman modes mostly affected by the different site occupancy are at ~110 cm^{-1}, ~193 cm^{-1}, ~520 cm^{-1}, and ~720 cm^{-1} (Fig. 10). To note, the barycenter of the IF band shifts linearly toward higher frequencies (+4.5 cm^{-1}) with the BCT/BZT ratio (see Fig. 11). Samples at 65 °C should have exclusively a tetragonal *P*4*mm* symmetry, according to the permittivity data shown in Fig. 8 and previous studies [18,21]. If this postulation is considered accurate, then the BCT content has a strong impact on many vibrations. In the LF region the most significant variations are the increased frequency splitting between bands, *e.g.,* the ~150 cm^{-1} and ~190 cm^{-1} modes. No variations are discernible in the ~293 cm^{-1} band. In the IF region, the shoulder at ~470 cm^{-1} increases its relative intensity for the lowest Zr contents, and in general, the barycenter of the whole IF region shifts to higher frequencies. By increasing the BCT/BZT ratio, the main band in the HF region moves nearly 6 cm^{-1} towards higher frequencies and there is a damping of the already small band at ~804 cm^{-1}. At the highest temperature of 130 °C, all samples are in the paraelectric phase. The bands are very broad and less intense. Remarkable variations due to the different site occupancies are observed in the IF region with the appearance of a more discernible contribution around 555 cm^{-1}, and an overall shift (~ +8 cm^{-1}) of the barycenter towards higher frequencies.

From the considerations reported above, it is clear that the shift of IF barycenter occurs in all compositions/symmetries, and the degree of frequency shift increases from BCZT40 to BCZT60 (Fig. 11). The IF barycenter for the five different compositions is shown in Fig. 11 and the linear fits of the IF barycenter for the five different compositions were used to generate three phase transition equations:

$$\text{Cubic phase boundary: } 520.6 + 0.4x \ (R^2 = 0.967) \quad (1)$$

$$\text{Tetragonal phase boundary: } 522.8 + 0.3x \ (R^2 = 0.916) \quad (2)$$

$$\text{Rhombohedral phase boundary: } 523.3 + 0.2x \ (R^2 = 0.924) \quad (3)$$

where x represents the BCT content. The validity of these equations is given by $40 < x < 60$. In turn, the provided phase transition equations could be used to estimate the phases by Raman spectroscopy, as long as the composition is within $40 < x < 60$. To test the validity of the proposed linear equations, the IF barycenter values of the room temperature samples were also plotted against the BCZT content in Fig. 11. It can be seen that despite the contribution of the *Amm*2 phase, there is a good agreement with the phase content calculated by XRD. For instance, samples BCZT55 and BCZT60 have respectively 45% and 67% *P*4*mm* phase content and the barycenter values are close to those collected at high temperatures for this symmetry. Therefore, the predominant presence of tetragonal phase can be estimated from the frequency position of the IF barycenter. The other three samples have lower barycenter values and fall in between the tetragonal-rhombohedral linear fits, in agreement with the XRD data, and the coexistence of an orthorhombic phase. Overall, the trend observed in the position of the barycenter for the room temperature samples is consistent with the deformation of the B-site by increasing the Zr/Ti ratio, and in turn, the increase in tetragonality. As a result, these equations could be used to provide an estimation of the symmetry in BCZT samples with BCT contents between 40 and 60, and collected under a variety of temperature and pressure conditions.

4. Conclusions

BCZT ceramic with different Ca/Ba and Zr/Ti molar ratios have been synthetized in order to gain a better understanding of the phase transitions and boundaries in such important materials. The coexistence of multiple phases at room temperature was observed by different techniques for all compositions. Data obtained from XRD, PDF analysis, and Raman spectroscopy allow to verify the octahedra distortion, *e.g.*, elongation and rotation, due to the Ti/Zr substitution, explaining the change in the symmetry as a function of composition. The changes in the

macroscopic dielectric properties show a good correlation with *in situ* temperature-dependent structural variations obtained via Raman spectroscopy within the temperature range of −60 °C to 130 °C. Indeed, the intensity ratio between the vibrational modes in the low and intermediate frequency ranges of the Raman spectra were used to identify the T_{T-O} and T_{O-R} as well as the ferroelectric phases and the paraelectric phase transitions. Furthermore, the barycenter of the main <Ti–O> stretching mode was used to provide phase transition equations that may be used to estimate the phase content by Raman spectroscopy. Additionally, the limited variation in the atomic interaction in the PDF analysis as a function of temperature can explain the diffuse phase transitions in BCZT40. This study provides essential information on the role of Ba/Ca and Ti/Zr substitution in the A- and B-site, respectively, in order to understand the direct effect on the crystal structure and phase transition of BCZT for further applications.

Declaration of Competing Interest

There are no conflicts to declare. The authors declare that they have no known competing financial interests or personal relationships that could have appeared to influence the work reported in this paper.

Acknowledgements

The authors gratefully acknowledge the financial support for this work from the Deutsche Forschungsgemeinschaft under Grant Nos. GRK2495/F, G, and H as well as HI 1867/1–2 and the Fraunhofer Internal Programs under grant no. Attract 40-04857. This research was financially supported by JSPS Japanese-German Graduate Externship (Grant No. 2019/R1). The authors would like to thank DESY German Electron Synchrotron for beamtime at the P02.1 beamline under proposal number I-20220124. Thanks are extended to the Japan Synchrotron Radiation Research Institute (JASRI) for the Total X-ray Scattering | PDF measurements that were performed at BL04B2 of SPring-8 under proposal numbers 2022A1549 and 2022B1415.

Appendix A. Supporting information

Supplementary data associated with this article can be found in the online version at doi:10.1016/j.jeurceramsoc.2024.03.003.

References

[1] B. Jaffe, Piezoelectric Ceramics, Elsevier Science, Saint Louis, 2014.
[2] K. Uchino. Ferroelectric Devices, 2nd Edition, Taylor and Francis, Hoboken, 2009.
[3] A.J. Moulson, J.M. Herbert. Electroceramics: Materials, Properties, Applications, Second edition, Wiley, New York, 2003.
[4] C.B. Carter, M.G. Norton. Ceramic Materials: Science and Engineering, Second edition, Springer, New York, 2013.
[5] Regulation (EC) No. 1907/2006 of the European Parliament and of the Council of 18 December 2006 concerning the Registration, Evaluation, Authorisation …, 2019.
[6] K.G. Webber, M. Vögler, N.H. Khansur, B. Kaeswurm, J.E. Daniels, F.H. Schader, Review of the mechanical and fracture behavior of perovskite lead-free ferroelectrics for actuator applications, Smart Mater. Struct. 26 (2017) 63001, https://doi.org/10.1088/1361-665X/aa590c.
[7] J. Rödel, W. Jo, K.T.P. Seifert, E.-M. Anton, T. Granzow, D. Damjanovic, Perspective on the development of lead-free piezoceramics, J. Am. Ceram. Soc. 92 (2009) 1153–1177, https://doi.org/10.1111/j.1551-2916.2009.03061.x.
[8] P. Kumari, Tiwari, Ashutosh, R. Rai, S. Sharma, M. Shandilya, a Ashutosh Tiwari, State-of-the-art of lead free ferroelectrics: a critical review, Adv. Mater. Lett. 6 (2015) 453–484, https://doi.org/10.5185/amlett.2015.4086.
[9] W. Liu, X. Ren, Large piezoelectric effect in Pb-free ceramics, Phys. Rev. Lett. 103 (2009) 257602, https://doi.org/10.1103/PhysRevLett.103.257602.
[10] Y. Bai, A. Matousek, P. Tofel, V. Bijalwan, B. Nan, H. Hughes, T.W. Button, Ba,Ca)(Zr,Ti)O3 lead-free piezoelectric ceramics—the critical role of processing on properties, J. Eur. Ceram. Soc. 35 (2015) 3445–3456, https://doi.org/10.1016/j.jeurceramsoc.2015.05.010.
[11] M. Acosta, N. Novak, W. Jo, J. Rödel, Relationship between electromechanical properties and phase diagram in the Ba(Zr0.2Ti0.8)O3–x(Ba0.7Ca0.3)TiO3 lead-free piezoceramic, Acta Mater. 80 (2014) 48–55, https://doi.org/10.1016/j.actamat.2014.07.058.
[12] D.R.J. Brandt, M. Acosta, J. Koruza, K.G. Webber, Mechanical constitutive behavior and exceptional blocking force of lead-free BZT- x BCT piezoceramics, J. Appl. Phys. 115 (2014) 204107, https://doi.org/10.1063/1.4879395.
[13] M.C. Ehmke, F.H. Schader, K.G. Webber, J. Rödel, J.E. Blendell, K.J. Bowman, Stress, temperature and electric field effects in the lead-free (Ba,Ca)(Ti,Zr)O 3 piezoelectric system, Acta Mater. 78 (2014) 37–45, https://doi.org/10.1016/j.actamat.2014.06.005.
[14] M. Acosta, N. Khakpash, T. Someya, N. Novak, W. Jo, H. Nagata, G.A. Rossetti, J. Rödel, Origin of the large piezoelectric activity in (1−x)Ba(Zr0.2Ti0.8)O3−x(Ba0.7Ca0.3)TiO3 ceramics, Phys. Rev. B 91 (2015), https://doi.org/10.1103/PhysRevB.91.104108.
[15] F. Cordero, F. Craciun, M. Dinescu, N. Scarisoreanu, C. Galassi, W. Schranz, V. Soprunyuk, Elastic response of (1 − x)Ba(Ti 0.8 Zr 0.2)O 3 – x (Ba 0.7 Ca 0.3) TiO 3 (x = 0.45–0.55) and the role of the intermediate orthorhombic phase in enhancing the piezoelectric coupling, Appl. Phys. Lett. 105 (2014) 232904, https://doi.org/10.1063/1.4903807.
[16] G.A. Rossetti, A.G. Khachaturyan, G. Akcay, Y. Ni, Ferroelectric solid solutions with morphotropic boundaries: vanishing polarization anisotropy, adaptive, polar glass, and two-phase states, J. Appl. Phys. 103 (2008) 114113, https://doi.org/10.1063/1.2930883.
[17] K. Fujita, Y. Ishibashi, Phase diagrams in successive phase transitions in ferroelectrics with Perovskite-type structure: cases of the first order transitions from the cubic phase, Jpn. J. Appl. Phys. 36 (1997) 5214–5218, https://doi.org/10.1143/JJAP.36.5214.
[18] D.S. Keeble, F. Benabdallah, P.A. Thomas, M. Maglione, J. Kreisel, Revised structural phase diagram of (Ba 0.7 Ca 0.3 TiO 3)-(BaZr 0.2 Ti 0.8 O 3), Appl. Phys. Lett. 102 (2013) 92903, https://doi.org/10.1063/1.4793400.
[19] I. Coondoo, N. Panwar, S. Krylova, A. Krylov, D. Alikin, S.K. Jakka, A. Turygin, V. Y. Shur, A.L. Kholkin, Temperature-dependent Raman spectroscopy, domain morphology and photoluminescence studies in lead-free BCZT ceramic, Ceram. Int. 47 (2021) 2828–2838, https://doi.org/10.1016/j.ceramint.2020.09.137.
[20] M.B. Abdessalem, S. Aydi, A. Aydi, N. Abdelmoula, Z. Sassi, H. Khemakhem, Polymorphic phase transition and morphotropic phase boundary in Ba1−x Ca x Ti1−y Zr y O3 ceramics, Appl. Phys. A 123 (2017), https://doi.org/10.1007/s00339-017-1196-7.
[21] A. Bjørnetun Haugen, J.S. Forrester, D. Damjanovic, B. Li, K.J. Bowman, J.L. Jones, Structure and phase transitions in 0.5(Ba 0.7 Ca 0.3 TiO 3)-0.5(BaZr 0.2 Ti 0.8 O 3) from −100 °C to 150 °C, J. Appl. Phys. 113 (2013) 14103, https://doi.org/10.1063/1.4772741.
[22] Le Zhang, M. Zhang, L. Wang, C. Zhou, Z. Zhang, Y. Yao, L. Zhang, D. Xue, X. Lou, X. Ren, Phase transitions and the piezoelectricity around morphotropic phase boundary in Ba(Zr 0.2 Ti 0.8)O 3 -x(Ba 0.7 Ca 0.3)TiO 3 lead-free solid solution, Appl. Phys. Lett. 105 (2014) 162908, https://doi.org/10.1063/1.4899125.
[23] D. Damjanovic, A. Biancoli, L. Batooli, A. Vahabzadeh, J. Trodahl, Elastic, dielectric, and piezoelectric anomalies and Raman spectroscopy of 0.5Ba(Ti 0.8 Zr 0.2)O 3 -0.5(Ba 0.7 Ca 0.3)TiO 3, Appl. Phys. Lett. 100 (2012) 192907, https://doi.org/10.1063/1.4714703.
[24] L. Da Lemos Silva, K.-Y. Lee, S. Petrick, M. Etter, A. Schökel, C.G. Chaves, N. Da Oliveira Silva, K.V. Lalitha, G. Picht, M.J. Hoffmann, M. Hinterstein, Uncovering the symmetry of the induced ferroelectric phase transformation in polycrystalline barium titanate, J. Appl. Phys. 130 (2021) 234101, https://doi.org/10.1063/5.0068703.
[25] Y.M. Jin, Y.U. Wang, A.G. Khachaturyan, J.F. Li, D. Viehland, Adaptive ferroelectric states in systems with low domain wall energy: tetragonal microdomains, J. Appl. Phys. 94 (2003) 3629–3640, https://doi.org/10.1063/1.1599632.
[26] J. Gao, D. Xue, Y. Wang, D. Wang, L. Zhang, H. Wu, S. Guo, H. Bao, C. Zhou, W. Liu, S. Hou, G. Xiao, X. Ren, Microstructure basis for strong piezoelectricity in Pb-free Ba(Zr 0.2 Ti 0.8)O 3 -(Ba 0.7 Ca 0.3)TiO 3 ceramics, Appl. Phys. Lett. 99 (2011) 92901, https://doi.org/10.1063/1.3629784.
[27] J. Gao, L. Zhang, D. Xue, T. Kimoto, M. Song, L. Zhong, X. Ren, Symmetry determination on Pb-free piezoceramic 0.5Ba(Zr 0.2 Ti 0.8)O 3 -0.5(Ba 0.7 Ca 0.3) TiO 3 using convergent beam electron diffraction method, J. Appl. Phys. 115 (2014) 54108, https://doi.org/10.1063/1.4864130.
[28] D. Damjanovic, A morphotropic phase boundary system based on polarization rotation and polarization extension, Appl. Phys. Lett. 97 (2010) 62906, https://doi.org/10.1063/1.3479479.
[29] D. Xue, Y. Zhou, J. Gao, X. Ding, X. Ren, A comparison between tetragonal-rhombohedral and tetragonal-orthorhombic phase boundaries on piezoelectricity enhancement, EPL 100 (2012) 17010, https://doi.org/10.1209/0295-5075/100/17010.
[30] Marco Deluca, Andreja Gajovic, Raman Spectroscopy of Nanostructured Ferroelectric Materials, in: Nanoscale Ferroelectrics and Multiferroics, John Wiley & Sons, Ltd, 2016, pp. 325–374.
[31] C.H. Perry, D.B. Hall, Temperature dependence of the Raman Spectrum of BaTi O3, Phys. Rev. Lett. 15 (1965) 700–702, https://doi.org/10.1103/PhysRevLett.15.700.
[32] N.K. Karan, R.S. Katiyar, T. Maiti, R. Guo, A.S. Bhalla, Raman spectral studies of Zr 4+ -rich BaZr x Ti 1− x O 3 (0.5⩽ x ⩽1.00) phase diagram, J. Raman Spectrosc. 40 (2009) 370–375, https://doi.org/10.1002/jrs.2134.
[33] V. Buscaglia, S. Tripathi, V. Petkov, M. Dapiaggi, M. Deluca, A. Gajović, Y. Ren, Average and local atomic-scale structure in BaZrxTi(1-x)O3 (x = 0. 10, 0.20, 0.40) ceramics by high-energy x-ray diffraction and Raman spectroscopy, J. Phys. Condens. Matter 26 (2014) 65901, https://doi.org/10.1088/0953-8984/26/6/065901.
[34] V.K. Veerapandiyan, M. Deluca, S.T. Misture, W.A. Schulze, S.M. Pilgrim, S. C. Tidrow, Dielectric and structural studies of ferroelectric phase evolution in

dipole-pair substituted barium titanate ceramics, J. Am. Ceram. Soc. 103 (2020) 287–296, https://doi.org/10.1111/jace.16713.
[35] N.H. Khansur, U.R. Eckstein, M. Bergler, A. Martin, K. Wang, J.-F. Li, M.R. Cicconi, K. Hatano, K. Kakimoto, D. de Ligny, K.G. Webber, In situ combined stress- and temperature-dependent Raman spectroscopy of Li-doped (Na,K)NbO 3, J. Am. Ceram. Soc. 105 (2022) 2735–2743, https://doi.org/10.1111/jace.18269.
[36] J. Schindelin, I. Arganda-Carreras, E. Frise, V. Kaynig, M. Longair, T. Pietzsch, S. Preibisch, C. Rueden, S. Saalfeld, B. Schmid, J.-Y. Tinevez, D.J. White, V. Hartenstein, K. Eliceiri, P. Tomancak, A. Cardona, Fiji: an open-source platform for biological-image analysis, Nat. Methods 9 (2012) 676–682, https://doi.org/10.1038/nmeth.2019.
[37] M. Herklotz, F. Scheiba, M. Hinterstein, K. Nikolowski, M. Knapp, A.-C. Dippel, L. Giebeler, J. Eckert, H. Ehrenberg, Advances in in situ powder diffraction of battery materials: a case study of the new beamline P02.1 at DESY, Hamburg, J. Appl. Cryst. 46 (2013) 1117–1127, https://doi.org/10.1107/S0021889813013551.
[38] Topas V4. 2: General profile and structure analysis software for powder diffraction data, 2009.
[39] Y. Tian, X. Chao, L. Jin, L. Wei, P. Liang, Z. Yang, Polymorphic structure evolution and large piezoelectric response of lead-free (Ba,Ca)(Zr,Ti)O 3 ceramics, Appl. Phys. Lett. 104 (2014) 112901, https://doi.org/10.1063/1.4868414.
[40] K. Brajesh, M. Abebe, R. Ranjan, Structural transformations in morphotropic-phase-boundary composition of the lead-free piezoelectric system Ba(Ti0.8Zr0.2)O3−(Ba0.7Ca0.3)TiO3, Phys. Rev. B 94 (2016) 104108, https://doi.org/10.1103/PhysRevB.94.104108.
[41] A. Veber, M.R. Cicconi, H. Reinfelder, D. de Ligny, Combined differential scanning calorimetry, Raman and Brillouin spectroscopies: a multiscale approach for materials investigation, Anal. Chim. Acta 998 (2018) 37–44, https://doi.org/10.1016/j.aca.2017.09.045.
[42] M.R. Cicconi, N.H. Khansur, U.R. Eckstein, F. Werr, K.G. Webber, D. Ligny, Determining the local pressure during aerosol deposition using glass memory, J. Am. Ceram. Soc. 103 (2020) 2443–2452, https://doi.org/10.1111/jace.16947.
[43] R.Y. Sato-Berrú, E.V. Mejía-Uriarte, C. Frausto-Reyes, M. Villagrán-Muniz, H.M. S, J.M. Saniger, Application of principal component analysis and Raman spectroscopy in the analysis of polycrystalline BaTiO3 at high pressure, Spectrochim. Acta Part A: Mol. Biomol. Spectrosc. 66 (2007) 557–560, https://doi.org/10.1016/j.saa.2006.03.032.
[44] N. Pisitpipathsin, P. Kantha, K. Pengpat, G. Rujijanagul, Influence of Ca substitution on microstructure and electrical properties of Ba(Zr,Ti)O3 ceramics, Ceram. Int. 39 (2013) S35–S39, https://doi.org/10.1016/j.ceramint.2012.10.031.
[45] M.R. Panigrahi, S. Panigrahi, Synthesis and microstructure of Ca-doped BaTiO3 ceramics prepared by high-energy ball-milling, Phys. B: Condens. Matter 404 (2009) 4267–4272, https://doi.org/10.1016/j.physb.2009.08.012.
[46] W. Cai, Q. Zhang, C. Zhou, R. Gao, F. Wang, G. Chen, X. Deng, Z. Wang, N. Deng, L. Cheng, C. Fu, Effects of oxygen partial pressure on the electrical properties and phase transitions in (Ba,Ca)(Ti,Zr)O3 ceramics, J. Mater. Sci. 55 (2020) 9972–9992, https://doi.org/10.1007/s10853-020-04771-8.
[47] Q. Zhang, W. Cai, C. Zhou, R. Xu, S. Zhang, Z. Li, R. Gao, C. Fu, Electric fatigue of BCZT ceramics sintered in different atmospheres, Appl. Phys. A 125 (2019) 1–9, https://doi.org/10.1007/s00339-019-3062-2.
[48] R.D. Shannon, Revised effective ionic radii and systematic studies of interatomic distances in halides and chalcogenides, Acta Cryst. A 32 (1976) 751–767, https://doi.org/10.1107/S0567739476001551.
[49] M. Otonicar, J. Park, M. Logar, G. Esteves, J.L. Jones, B. Jancar, External-field-induced crystal structure and domain texture in (1−x)Na0.5Bi0.5TiO3–xK0.5Bi0.5TiO3 piezoceramics, Acta Mater. 127 (2017) 319–331, https://doi.org/10.1016/j.actamat.2017.01.052.
[50] R. Bhattacharyya, S. Das, S. Omar, High ionic conductivity of Mg2+-doped non-stoichiometric sodium bismuth titanate, Acta Mater. 159 (2018) 8–15, https://doi.org/10.1016/j.actamat.2018.08.007.
[51] A. Gadelmawla, K. Riess, J. Birkenstock, M. Hinterstein, K.G. Webber, N. H. Khansur, Effect of varying Bi content on the temperature-dependent mechanical, dielectric, and structural properties of nominal Na 1/2 Bi 1/2 TiO 3, J. Appl. Phys. 130 (2021) 185106, https://doi.org/10.1063/5.0070594.
[52] B.-C. Shin, H.-G. Kim, Dielectric breakdown and partial disc0harge in batio 3 ceramics, Ferroelectrics 89 (1989) 81–86, https://doi.org/10.1080/00150198908017886.
[53] C. Baek, J.E. Wang, S. Moon, C.-H. Choi, D.K. Kim, Formation and accumulation of intragranular pores in the hydrothermally synthesized barium titanate nanoparticles, J. Am. Ceram. Soc. 99 (2016) 3802–3808, https://doi.org/10.1111/jace.14397.
[54] G. Dale, M. Strawhorne, D.C. Sinclair, J.S. Dean, Finite element modeling on the effect of intra-granular porosity on the dielectric properties of BaTiO 3 MLCCs, J. Am. Ceram. Soc. 101 (2018) 1211–1220, https://doi.org/10.1111/jace.15261.
[55] M.C. Ehmke, S.N. Ehrlich, J.E. Blendell, K.J. Bowman, Phase coexistence and ferroelastic texture in high strain (1−x)Ba(Zr 0.2 Ti 0.8)O 3 –x(Ba 0.7 Ca 0.3)TiO 3 piezoceramics, J. Appl. Phys. 111 (2012) 124110, https://doi.org/10.1063/1.4730342.
[56] S. Zhukov, M. Acosta, Y.A. Genenko, H. von Seggern, Polarization dynamics variation across the temperature- and composition-driven phase transitions in the lead-free Ba(Zr 0.2 Ti 0.8)O 3 −x(Ba 0.7 Ca 0.3)TiO 3 ferroelectrics, J. Appl. Phys. 118 (2015) 134104, https://doi.org/10.1063/1.4932641.
[57] S. Tinte, M.G. Stachiotti, M. Sepliarsky, R.L. Migoni, C.O. Rodriguez, Order-disorder, local structure and precursor effects in BaTiO 3, Ferroelectrics 237 (2000) 41–48, https://doi.org/10.1080/00150190008216230.
[58] C. Laulhé, F. Hippert, R. Bellissent, A. Simon, G.J. Cuello, Local structure in BaTi1−xZrxO3 relaxors from neutron pair distribution function analysis, Phys. Rev. B 79 (2009) 64104, https://doi.org/10.1103/PhysRevB.79.064104.
[59] I. Levin, V. Krayzman, J.C. Woicik, Local-structure origins of the sustained Curie temperature in (Ba,Ca)TiO 3 ferroelectrics, Appl. Phys. Lett. 102 (2013) 162906, https://doi.org/10.1063/1.4802996.
[60] Y. Yoneda, K. Suzuya, J. Mizuki, S. Kohara, Local structure of relaxor Pb(In0.5Nb0.5)O3 ferroelectrics, J. Appl. Phys. 100 (2006), https://doi.org/10.1063/1.2358819.
[61] D. Hou, T.-M. Usher, H. Zhou, N. Raengthon, N. Triamnak, D.P. Cann, J. S. Forrester, J.L. Jones, Temperature-induced local and average structural changes in BaTiO 3 − x Bi(Zn 1/2 Ti 1/2)O 3 solid solutions: The origin of high temperature dielectric permittivity, J. Appl. Phys. 122 (2017) 64103, https://doi.org/10.1063/1.4989393.
[62] C.M. Culbertson, A. Manjón-Sanz, M. Lucero, Z. Feng, M.R. Dolgos, The local structure of 0.5Ba(Zr0.2Ti0.8)O3-0.5(Ba0.7Ca0.3)TiO3 from neutron total scattering measurements and multi-edge X-ray absorption analysis, Mater. Res. Bull. 135 (2021) 111124, https://doi.org/10.1016/j.materresbull.2020.111124.
[63] J.G. Park, T.S. Oh, Y.H. Kim, Dielectric properties and microstructural behaviour of B-site calcium-doped barium titanate ceramics, J. Mater. Sci. 27 (1992) 5713–5719, https://doi.org/10.1007/BF01119727.
[64] C.M. Culbertson, A.T. Flak, M. Yatskin, P.H.-Y. Cheong, D.P. Cann, M.R. Dolgos, Neutron total scattering studies of group II titanates (ATiO3, A2+ = Mg, Ca, Sr, Ba), Sci. Rep. 10 (2020) 3729, https://doi.org/10.1038/s41598-020-60475-8.
[65] M. Ghita, M. Fornari, D.J. Singh, S.V. Halilov, Interplay between A -site and B -site driven instabilities in perovskites, Phys. Rev. B 72 (2005) 54114, https://doi.org/10.1103/PhysRevB.72.054114.
[66] A. Gadelmawla, U. Eckstein, K. Riess, Y.-X. Liu, K. Wang, J.-F. Li, K. Kakimoto, N. H. Khansur, K.G. Webber, Temperature- and stress-dependent electromechanical properties of phase-boundary-engineered KNN-based piezoceramics, jace.18917, J. Am. Ceram. Soc. (2022), https://doi.org/10.1111/jace.18917.
[67] A. Gadelmawla, D. Dobesh, U. Eckstein, O. Grübl, M. Ehmke, M.R. Cicconi, N. H. Khansur, D. de Ligny, K.G. Webber, Influence of stress on the electromechanical properties and the phase transitions of lead-free (1 − x)Ba(Zr0.2Ti0.8)O3–x(Ba0.7Ca0.3)TiO3, J. Mater. Sci. 57 (2022) 16581–16599, https://doi.org/10.1007/s10853-022-07685-9.
[68] R. Farhi, M. El Marssi, A. Simon, J. Ravez, A Raman and dielectric study of ferroelectric ceramics, Eur. Phys. J. B 9 (1999) 599–604, https://doi.org/10.1007/s100510050803.
[69] A. Hamza, F. Benabdallah, I. Kallel, L. Seveyrat, L. Lebrun, H. Khemakhem, Effect of rare-earth substitution on the electrical properties and Raman spectroscopy of BCTZ ceramics, J. Alloy. Compd. 735 (2018) 2523–2531, https://doi.org/10.1016/j.jallcom.2017.11.351.
[70] Z. Hanani, D. Mezzane, M. Amjoud, A.G. Razumnaya, S. Fourcade, Y. Gagou, K. Hoummada, M. El Marssi, M. Gouné, Phase transitions, energy storage performances and electrocaloric effect of the lead-free Ba0.85Ca0.15Zr0.10Ti0.90O3 ceramic relaxor, J. Mater. Sci: Mater. Electron 30 (2019) 6430–6438, https://doi.org/10.1007/s10854-019-00946-5.
[71] S. Merselmiz, Z. Hanani, D. Mezzane, A.G. Razumnaya, M. Amjoud, L. Hajji, S. Terenchuk, B. Rožič, I.A. Luk'yanchuk, Z. Kutnjak, Thermal-stability of the enhanced piezoelectric, energy storage and electrocaloric properties of a lead-free BCZT ceramic, RSC Adv. 11 (2021) 9459–9468, https://doi.org/10.1039/D0RA09707A.
[72] G. Arlt, D. Hennings, G. de With, Dielectric properties of fine-grained barium titanate ceramics, J. Appl. Phys. 58 (1985) 1619–1625, https://doi.org/10.1063/1.336051.